Accepted ms, GEM International Journal on Geomathematics doi:10.1007/s13137-020-00158-8

# Heterogeneity-controlled uncertain optimization of pump-and-treat systems explained through geological entropy

Daniele Pedretti

Dipartimento di Scienze della terra "A. Desio", Università degli Studi di Milano, Milan, Italy

(daniele.pedretti@unimi.it)

## Abstract

Pump-and-treat (P&T) is a widely-adopted solution for the containment of solute plumes in contaminated aquifers. A cost-effective design of P&T systems requires optimizing (minimizing) the overall pumping rates ($Q$) . This optimization is a stochastic process, as $Q$ is a random variable linked to the randomness of the aquifer hydraulic conductivity ($K$). Previously presented stochastic approaches to minimize $Q$ adopted two-dimensional (2D) Gaussian random spatial fields (r.s.f.) of log-transformed $K$. Recent studies based on geological entropy have demonstrated the limited ability of Gaussian r.s.f. to reproduce extreme $K$ patterns, which mostly control transport in heterogeneous aquifers, when compared to non-Gaussian r.s.f. Moreover, 2D models generate different flow and transport connectivity than three-dimensional (3D) models. On these premises, this work aimed at extending previous works on P&T optimization in heterogeneous aquifers through Monte-Carlo groundwater simulations of 2D and 3D Gaussian and non-Gaussian r.s.f. The results indicated that the mean ($\overline{Q_n}$) and variance ($\sigma^2_{Qn}$) of the optimal $Q$ distribution depend strictly on the chosen model dimensionality and r.s.f. generator. In particular, 2D models and models embedding indicator-based (i.e. non-Gaussian) r.s.f. tended to generate higher

$\overline{Q_n}$ and $\sigma^2_{Qn}$ than 3D models with increasing number of model layers ($N_L$) and Gaussian models. This behavior can be explained considering the spatial ordering of $K$ clusters in the simulated aquifers, which is measured through metrics derived from the concept of geological entropy. It was found that 2D models and models embedding non-Gaussian r.s.f. displayed more spatially-persistent ordered $K$ structures than 3D models and Gaussian models, resulting in higher $\overline{Q_n}$ and $\sigma^2_{Qn}$ . This is attributed to the relative amount of heterogeneity sampled by the solute source and the increased likelihood of more ordered $K$ clusters to generate preferential flow and solute transport channeling than more disordered and chaotic systems, which enhance solute mixing. Combining P&T with physical barriers (i.e. cut-off walls) was helpful to reduce both $\overline{Q_n}$ and $\sigma^2_{Qn}$ in all tested scenarios, corroborating previous findings. However, the relative efficacy of a specific physical barrier geometry to reduce $\overline{Q_n}$ and $\sigma^2_{Qn}$ also depends on the chosen model dimensionality and r.s.f. generator.

*Keywords: aquifer heterogeneity, solute plume containment, pump-and-treat, stochastic modeling, geological entropy, cost-effective analysis.*

# 1 Introduction

Pump-and-treat (P&T) is a widespread technique for solute plume management (e.g. Mackay and Cherry, 1989; EPA, 2005; Pedretti *et al.*, 2013b; Beretta, 2015). Despite the decadal use of this technique and the emergence of alternative solutions for remediation purposes (e.g. Kuppusamy *et al.*, 2016), P&T remains widely adopted for the containment of solute plumes (e.g. Truex *et al.*, 2015; Pedretti *et al.*, 2017; Casasso *et al.*, 2020). This is mainly due to the relatively easy design of P&T systems, which conventionally includes one or more pumping wells located downstream of the detected plume and a facility for water treatment. The principle of P&T as a containment system is based on the formation of a well

capture zone which collects the solute particles migrating from upstream of one or multiple wells, which form a hydraulic barrier (e.g. (Pedretti *et al.*, 2013b). If the P&T is correctly tuned, the well capture zone is large enough to intercept the plume and all solute particles are collected by the hydraulic barrier. Otherwise, some solute particles can escape the well capture zone, creating a threat for groundwater resources located downstream of the hydraulic barrier.

The cost of unit volume of treated water, which depends directly on the overall pumping rate of the hydraulic barrier, $Q$, represents a critical aspect to consider for a cost-effective design of a P&T system (e.g. Bayer *et al.*, 2005). A 2001 study by U.S. EPA summarized remediation costs of 48 sites in the U.S., suggesting an average 4.9 Million USD as capital (i.e. installation) costs per facility, 82.5 USD/year as operating costs per $m^3$ of pumped groundwater, averaging 31700 $m^3$/year and an average 6 years of system operations (e.g. Wiegand & Shanahan, 2001). Using these reference values, the total operational cost of a single facility run for 6 years would be about 225 Million USD, i.e. 45 times larger than the initial capital costs, stressing the importance of minimizing $Q$ to reduce the running costs of a P&T systems.

Multiple physical and mathematical solutions have been proposed to reduce or minimize $Q$. From a physical perspective, P&T hydraulic barriers can be combined with physical barriers, such as low-permeable cutoff walls or diaphragms (e.g. Dominijanni *et al.*, 2017; Pedretti *et al.*, 2017; Yang *et al.*, 2020). Compared to "conventional" (i.e., physical-barrier-free) P&T systems, a "combined" P&T system is expected to decrease $Q$, as the physical barrier reduces the seepage flow between the solute plume source and the hydraulic barriers, while funneling the contaminant plume towards the extraction wells (e.g. Bayer et al., 2004). From a mathematical perspective, several analytical (e.g. Javandel and Tsang,

1986) and numerical (e.g. Wang and Zheng, 1997) algorithms can be used to find optimal pumping rates that ensure collecting the entire contaminant plume with the minimum $Q$.

In complex heterogeneous formations, minimizing $Q$ remains an uncertain task. As transport processes occur over multiple spatial scales which are usually difficult to characterize, the hydraulic parametrization of aquifers is usually incomplete, generating epistemic uncertainty (Tartakovsky, 2013). This is particularly true for key aquifer parameters that strongly controls the migration of solute transport in aquifers, such as the aquifer hydraulic conductivity, $K$, which can fluctuate over several order of magnitude within short spatial scales (e.g. Freeze, 1975; Sanchez-Vila *et al.*, 2006). This issue severely complicates the decision-making process by regulators and administrations dealing with the containment of solute plumes using P&T, as the variability in hydrogeological parameters (particularly $K$) generates uncertainty in the decision-making process. Stochastic modeling, such as Monte Carlo (MC) simulations based on geostatistical modeling, can assist decision makers relying on model-based decisions when dealing with heterogeneity-driven uncertainty (e.g. Rubin *et al.*, 1994; Freeze, 2004; Tartakovsky, 2013; Pedretti *et al.*, 2017, 2020).

Bayer et al. (2004) presented one of the first documented MC-based numerical analyses for the optimization of P&T systems under heterogeneity-driven uncertainty. They created two-dimensional (2D) Sequential Gaussian Simulations (SGS) of the log-transformed hydraulic conductivity ($Y = \ln K$). They simulated scenarios of correlated random spatial fields (r.s.f) with increasing variance $\sigma_Y^2$ and correlation (integral) scales $I_Y$, which were used to parametrize groundwater flow models, in turn used to perform particle tracking simulations. By targeting different $\sigma_Y^2$ and $I_Y$ values, Bayer et al. (2004) aimed at testing the response of P&T in aquifers with different hydrogeological settings. Moreover, Bayer et al. (2004) considered different "combined" P&T configurations by changing the geometry of

the physical barriers located at different distances between the pumping wells and the contaminant source. Among the key results, Bayer et al. (2004) found that the uncertainty around the minimum $Q$ was strongly controlled by $I_Y$ and $\sigma_Y^2$, as well as by the geometry of physical barriers: simulations with higher $I_Y$ ($\sigma_Y^2$) resulted in stronger uncertainty than simulations with lower $I_Y$ ($\sigma_Y^2$). The presence of physical barriers generally reduced the mean $Q$, while the uncertainty around the mean depended on the type of physical barriers. These conclusions were further corroborated by a follow-up study (Bayer and Finkel, 2006).

In the recent years, questions have been posed regarding the actual ability of Gaussian-based models to effectively reproduce solute transport in heterogeneous aquifers. There is a growing consensus that reconstructed spatial fields created using Gaussian-based stochastic simulator may not honor the structure of extreme $K$ patterns observed in real-life aquifer, which strongly control transport in heterogeneous media (e.g. Journel and Deutsch, 1993; Gómez-Hernandez and Wen, 1998; Zinn and Harvey, 2003; Pedretti *et al.*, 2013a; Bianchi and Pedretti, 2018). Several studies have shown that non-Gaussian approaches allow reproducing the structured and connected $K$ patterns of natural aquifers. In particular, non-Gaussian models can generate r.s.f that closely mimic the connected nature of lithological facies in geological media, such as connected gravel and sands paleo-channels or water-bearing fractures. Non-Gaussian r.s.f can be obtained through multiple approaches, such as indicator-based simulations (e.g. Carle and Fogg, 1997; Sartore *et al.*, 2016) or multiple-point geostatistics (e.g. Strebelle, 2002).

Another relevant aspect when dealing with solute transport modeling is the chosen model dimensionality. Several studies showed that the scaling of contaminants in space and time depends directly on the selected model dimensionality. For instance, the numerical tracer tests under radial convergent flow in SGS-based fields (Pedretti *et al.*, 2013a) showed that

breakthrough curves obtained from 2D fields characterized by the same geostatistics as 3D fields did not generate the typical *anomalous* or *non-Fickian* patterns associated to transport in heterogeneous media, such as breakthrough curves tailing. On the contrary, 3D SGS simulations were able to generate non-Fickian transport, remaking the fundamental difference in transport patterns depending on the selected model dimensionality under non-uniform flow configurations. One reason explaining the difference between transport in 2D and 3D r.s.f. is the different percolation thresholds characterizing the fields (e.g. Berkowitz and Balberg, 1993; Silliman, 1996), which affect the resulting flow and transport connectivity of the system (e.g. Fiori and Jankovic, 2012; Bianchi and Pedretti, 2018). A second reason is related to the relative size of the plume source (i.e. size of the injection line or block) compared to the amount of heterogeneity sampled by the source in the vertical direction (e.g. Pedretti *et al.*, 2014), which may chance between 2D and 3D simulations.

In the recent years, new metrics to describe the spatial structures of heterogeneous fields have emerged. One of them is geological entropy (Bianchi and Pedretti, 2017, 2018), an approach that improves the description of heterogeneous aquifers compared to classic variogram-based indicators (see also Section 2). Based on Shannon's information entropy theory (Shannon, 1948), geological entropy is useful to measure the spatial order of categorical variables describing hydrogeological parameters, such as the lithofacies characterized by discrete $K$ values. Simple metrics derived from geological entropy can be correlated to characteristic features of flow and solute transport in porous and fractured media, such as the temporal moments of the solute transport evaluated in control wells (i.e. the solute breakthrough curves) (Bianchi and Pedretti, 2017; Pedretti and Bianchi, 2019).

This work extends the Monte Carlo (MC) analyses by Bayer et al. (2004) to evaluate the optimal use of P&T using 2D and 3D stochastic numerical modeling embedding both Gaussian and non-Gaussian r.s.f. The work has two overarching aims.

1) The first aim is to showcase the importance of selecting a specific model configuration (2D or 3D, Gaussian and non-Gaussian) for the numerical optimization of a P&T. To this end, we adopted a similar model setup presented by Bayer et al. (2004) and performed a scenario-based MC analysis simulating conventional and combined P&T configurations in 2D and 3D, Gaussian and non-Gaussian r.s.f. with increasing number of layers ($N_L$). For each combination of parameters, we calculated the first two moments (mean and variance) of the ensemble of resulting optimal pumping rates from each scenario. The difference in these moments among the tested scenarios are then analyzed and discussed.
2) The second aim is to use geological entropy to interpret the results. In particular, we evaluate if two metrics derived from geological entropy, the entrogram scale $H_s$ and the local relative entropy $H_{R0}$ (mathematically defined in the Section 3.4), can explain the results for each P&T scenario. Geological entropy has not been rigorously applied yet to explore flow and transport under non-uniform (bounded) aquifer conditions, which is the case of P&T systems. This issue further motivates this study.

# 2 Background

We briefly revise some of the salient aspects of Bayer et al. (2004), hereafter "B2004", and of geological entropy, which provide the background study for this analysis.

## 2.1 Bayer et al. (2004)

B2004 performed a parametric MC analysis based on numerical groundwater flow modeling and particle tracking analysis. Two-dimensional (i.e. $N_L$=1) numerical flow models were generated using the block-centered finite difference code MODFLOW-88

(McDonald and Harbaugh, 1988). The model had quadratic dimensions of $L_X$=300m and $L_Y$=300m and was oriented parallel to the Cartesian coordinates (*x,y*). The model had unit thickness ($L_Z$=1m). The system was discretized using a uniform unit-size space grid, resulting in a $300 \times 300 \times 1$ cells. Steady-state flow was simulated assuming confined conditions and a regional flow gradient $i = 0.001$ parallel to the y-coordinate. Prescribed head (Dirichlet) boundary conditions were set at the top and bottom boundaries. No-flow (Neuman) boundary conditions were set at the lateral boundaries. Particle tracking were performed using the code MODPATH (Pollock, 1994). They assumed an instantaneous injection of particles (mimicking the discretized solute mass) released from a quadratic zone with dimensions $H_S$=50 m × $W_S$=50 m. The closest edge of the source area was located at a variable distance $r$ from a pumping well, with pumping rate $Q$.

Five different P&T scenarios were considered in the work by B2004. Scenario "A" (Figure 1, top-right panel) considered a "conventional" P&T scheme with no physical barriers. Scenario "B" and "C" (Figure 1, bottom-left panel) considered "combined" schemes, with one physical barrier respectively located upstream and downstream of the source area. Scenario "D" considered a double upstream and downstream barrier. Scenario "E" (Figure 1, bottom-right panel) considered a barrier located upstream of the source and two lateral barriers at the left and right sides of the source. These P&T scenarios were tested in homogeneous and heterogeneous synthetic aquifers. The heterogeneous simulations were performed using SGS. Treating $Y$ as a correlated Gaussian r.s.f. with zero mean ($\bar{Y}$=0), four sets of simulations were obtained imposing two-point isotropic exponential covariance functions of $Y$, $C_Y$, of form

$$C_Y(\boldsymbol{h}) = \sigma_Y^2 \exp\left(\frac{-|\boldsymbol{h}|}{I_Y}\right) \qquad (1)$$

where $\boldsymbol{h}$ is the lag vector between two points. They set variable integral scales (up to $I_Y = 1.53\, W_s$) and variances (up to $\sigma_Y^2 = 1.8$). B2004 generated a total of $N_{MC}$= 500 unconditional r.s.f. fields, and for each combination of parameters listed in Table 1 they resolved flow and transport in each realization.

For $Q = 0$, the particles were allowed to leave the aquifer from the lower boundary (i.e. at y=0). For $Q > 0$ the pumping well generated a capture zone that tended to collect the particles, thus acting as a hydraulic barrier. For increasing $Q$, the well had higher chance to collect the entire particle distributions than for $Q \to 0$. An optimal pumping rate ($Q_{opt}$) was defined as the minimum pumping rate that allow the well collecting the whole particle cloud. A distribution of normalized optimal pumping rates ($Q_n$, mathematically defined in Section 3.5) was obtained from the ensemble of the $N_{MC}$ realizations resolved for each combination of parameters. The first ($\overline{Q_n}$) and second ($\sigma_{Qn}^2$) moments of the distributions were used as metrics to evaluate and analyze the differences among the tested combinations of parameters.

The analyses by B2004 concluded that the ensemble of $Q_{opt}$ was differently sensitive to the parameters listed in Table 1. Key results from the reference study worth noticing for the sake of the present study are the following:

- Variograms-based indicators $I_Y$ and $\sigma_Y^2$ had a dominant effect on the average $Q_{opt}$. Systems with higher $I_Y$ and $\sigma_Y^2$ required, on average, larger $\overline{Q_n}$ to capture all the particles. Variogram-based indicators had also a dominant effect on the uncertainty of optimal pumping rates, measured by $\sigma_{Qn}^2$. This was associated to the channeling effects of solute transport in the systems, which increased for higher $I_Y/\mathrm{L_x}$ ratios and for increasing $\sigma_Y^2$ (the latter determining a higher chance of increasingly larger $K$ values).

- Both $\overline{Q_n}$ and $\sigma^2_{Qn}$ were generally reduced when using physical barriers coupled to the hydraulic barrier.
- Certain types of physical barrier generated more reductions on the mean and uncertainty than others. The best scenario in terms of expected (mean) and uncertainty (variance) of the optimal pumping rates was obtained for scenario "E", when the total length of the physical barriers was set to three times the plume width (Figure 1).

## 2.2 Geological entropy

Geological entropy (Bianchi and Pedretti, 2017, 2018) is an approach to explore and measure the spatial ordering of the classes of geological parameters over a three-dimensional domain of interest. The principle of geological entropy is based on Shannon's information entropy theory (Shannon, 1948), which is routinely used in statistical analysis - including (hydro)geological applications - to quantify the uncertainty of correlated or uncorrelated spatially-distributed variables (e.g. Journel and Deutsch, 1993; Scheibe, 1993; Mays *et al.*, 2002; Pham, 2010; Huang *et al.*, 2012; Bianchi *et al.*, 2015; Pham and Yan, 2018). Among the previous studies using information entropy in hydrogeology, Journel and Deutsch (1993) presented a spatial entropy approach to show that multi-Gaussian models typically maximize the spatial disorder in the r.s.f. , but that this does not entail maximum entropy of the model outputs. This issue is key for risk assessment and solute transport modeling, which requires the full range of possible concentration outcomes from the models, particularly the highest (extreme) values leading to larger exposure to a specific contaminant.

Bianchi and Pedretti (2017, 2018) presented an algorithm to compute the relative proportion of a facies within subdomains of increasing size (the approach is mathematically

defined in the section 3.4). Compared to the spatial entropy algorithm by Journel and Deutsch (1993), the peculiarity of geological entropy is that the occurrence of the outcomes of a facies proportion within the subdomain is considered as an independent event. Noticing that the algorithm is general and any categorical or continuous hydrogeochemical parameter could be used as an input (including $K$, porosity, storage coefficients or biochemical reaction rates), Bianchi and Pedretti (2017, 2018) used this method to evaluate the Shannon entropy of "hydrofacies", i.e. the classes forming the lithofacies and parametrized by $K$, at increasing scales. Well-defined correlations were obtained between characteristic geological entropy metrics defining the hydrofacies and characteristics metrics defining solute transport in highly heterogeneous media. Specifically, Bianchi and Pedretti (2017, 2018) showed that geological entropy metrics can predict non-Fickian transport behaviour in alluvial aquifers from knowledge of physical heterogeneity. Stochastic simulations of tracer tests were conducted in synthetic $K$ fields based on realistic distributions of hydrofacies in alluvial aquifers are conducted to identify empirical relations between geological entropy metrics and the temporal moments of the resulting breakthrough curves (BTCs). Bianchi and Pedretti (2017, 2018) concluded that geological entropy performed better than classic stochastic indicators used to describe the heterogeneity of aquifers, such as two-point variograms fully characterized in terms of $I_Y$ and $\sigma_Y^2$ (e.g. Dagan, 1989). The results of Bianchi and Pedretti (2017, 2018) agree with the conclusions from other studies, including Zinn and Harvey (2003), who showed that Gaussian r.s.f .characterized by identical $I_Y$ and $\sigma_Y^2$ but different connectivity of $K$ patterns can generate different spatio-temporal scaling of solute plumes, invalidating the use of $I_Y$ and $\sigma_Y^2$ as good descriptors of solute transport.

# 3 Methodology

The model setup by B2004, presented in Section 2, is inherited in this work and extended to simulate flow and transport in three-dimensional (3D) Gaussian and non-Gaussian stochastic fields. We start explaining the extension from 2D to 3D for the homogeneous setup, and then the heterogeneous setup embedding the new geostatistical simulations. We then define the P&T scenarios analyzed in this work and introduced the geological entropy metrics that allow measuring the spatial ordering of the generated random spatial fields. Ultimately, we define the dimensionless variables that allow comparing the results among different model configurations.

## 3.1 Homogeneous model setup

In the homogeneous configuration, all $K$values in the model were locally isotropic and equal to $K$=1 m/d. For the 2D model, a single layer with thickness $b$=1 m constant in all points was used. We placed $N_p$=200 particles regularly distributed as in a square, as conceptually shown in Figure 1, mimicking the source geometry and size adopted by B2004. We kept the same boundary conditions and gradient as in the reference study. Flow was resolved using the code MODFLOW 2000 (Harbaugh *et al.*, 2000) and particle tracking using RW3D (e.g. Fernàndez-Garcia *et al.*, 2005).

In the 3D model configuration, the number of layers $N_L$ was increased to $N_L$=10,25 and 50. Using unit-thickness layers, the resulting aquifer thickness $B$ was $B = \sum N_L$. The overall transmissivity is therefore calculated as $T=KB=\sum N_L$. Keeping the same $x,y$ coordinates of the source location in 2D, we placed an equivalent amount of particles $N_p$ in all layers forming the 3D model, resulting in a total number of particles $p_{all} = N_p \times N_L$.

A fully-penetrating pumping well, with constant pumping rate $Q$, was set up at the center of domain along the x-axis, at a planar distance $r$ from the closest edge of the source (Figure 1). As in the reference work by B2004, the well acted as the sole hydraulic barrier, and $Q_{opt}$ was defined as the minimum pumping rate required for complete plume control, i.e. all $p_{all}$ particles released from the squared zone collected by the well.

A simple iterative approach for the optimization process was adopted. Starting from an initial value $Q$, an initial differential increment in pumping rates $dQ$ was set, such that

$$Q(i+1,\mathrm{j}) = Q(i,j) + dQ(j) \tag{2}$$

where $i$ is the number of the iteration ($i = 1, \dots, N$), and $j$ is the repetition of the iterative process ($j = 1, \dots, J$). For $j = 1$, the flow problem embedding $Q(i+1,1)$ was resolved, particle tracking performed and the number of particles collected by pumping well ($p_w$) was counted. While $p_w < p_{all}$, the iteration was repeated $N$ times until $p_w = p_{all}$. When this occurred at the $N$ iteration, the pumping rate to the previous iteration, i.e. $Q(N-1,1)$, was stored and used as the initial $Q$ for the round of iterations ($j = j+1$), while the increment $dQ$ was divided by a factor 10, i.e.

$$\begin{aligned} dQ(j+1) &= 0.1\, dQ(j) \\ Q(i=1,j+1) &= Q(N-1,j) + dQ(j+1) \end{aligned} \tag{3}$$

The process was repeated $J$ times until a desired precision in the optimal pumping rates is found. Here, we adopted $Q(i=1,j=1)=1$, $dQ(p=1)=1$ and $J=3$, such at the minimum $dQ = 0.001$. In other words, we obtained the estimation of the optimal pumping rates with an error of 0.1% of the initial $dQ$. The final optimal pumping rate resulting from the iterative process is then

$$Q_{opt} = Q(N, \mathrm{J}). \quad (4)$$

## 3.2 Heterogeneous setup

The first approach to generate stochastic heterogeneous fields of $Y$ was based on Sequential Gaussian Simulation (SGS), coded in SGEMS (Remy *et al.*, 2009). The simulations were based on the same isotropic covariance functions used by B2004 (Equation 1) and identical to 2D and 3D configurations. A random field generated using the SGS approach is shown in Figure 2a (left). We note that the use of an isotropic covariance function for the 3D models implied that the resulting r.s.f. had the same variance and correlation length in the horizontal plane ($I_{Y(h)}$) and in the vertical direction ($I_{Y(z)}$). In turn, this implies that the relative ratio $I_{Y(z)}/L_z$ decreases as the vertical domain size increases. The importance of this selection on the model results is discussed in the remaining of this paper.

The second approach was based on the non-Gaussian Sequential Indicator Simulation (SIS) (e.g. Deutsch & Journel, 1998; Emery, 2004; Soares, 1998), also coded in SGEMS. We imposed identical covariance function as in the SGS models and ensured reproduction of the global proportions of each category by binning the multivariate Gaussian $Y$ probability density function (pdf) characterized by zero mean and specific variance used in the SGS simulations. Binning implied discretizing the pdf into $N_C$ classes, ensuring that the same overall empirical variance of the $Y$ fields was maintained using SGS and SIS algorithms. After some initial trials, we found $N_C$=10 as a suitable working value. A random field generated using the SIS approach is shown in Figure 2a (right).

In B2004, all 2D simulations were unconditional, i.e. not conditioned to hard or soft data. The well pumping rate was fixed at a MODFLOW cell and a single $Q$ value (a Neuman BC) was imposed. In 3D modelling, the well intercepted multiple layers, and $Q$ must be

distributed along the cells forming the well's vertical column. Under homogeneous 3D conditions, $Q$ could be uniformly split into the number of layers forming the vertical column, i.e. $Q_k = Q/N_L$ $(k = 1, \dots, N_L)$. Under heterogeneous 3D conditions, this approach was no longer valid, as a uniform distribution of pumping rates across the layers would force the model to pump water out from any cells, including those characterized by low $K$. Splitting $Q$ using a deterministic weighting approach, such as based on the local $K$ intercepted by the well cells, seemed also not fully accurate, as the net pumping efficiency of a system depended not only on the specific $K$ cells where the pump is located, but also on the cluster of adjacent cells surrounding the pumping cell. We thus opted to generate conditional stochastic simulations, where the sole hard data conditioning the fields were imposed along at the well location. Specifically, we set a fixed hydraulic conductivity $K$=10 m/d in the cells forming the entire well column, and then assigned a uniform pumping rate to each cell. We tested conditional and unconditional scenarios for the 2D models and found minor deviations in terms on means and variance of the optimal pumping rates. As such, we adopted well conditioning throughout the entire work presented here.

## 3.3 Tested scenarios

For each stochastic simulation (SGS and SIS) and number of layers ($N_L$=1, 10, 25 and 50), we reproduced three of the five P&T scenarios presented by B2004 (Figure 1):

- Scenario "A" – "conventional" P&T with no physical barriers.
- Scenario "C" – "combined" P&T with downgradient barrier.
- Scenario "E" – "combined" P&T with upgradient and side barriers.

The selection was made considering that Scenario "A" and "E" were the worst and best scenarios (respectively) in terms of P&T efficiency, according to the work by B2004. Scenario "C" was chosen as an intermediate scenario between A and E, being a common

simple geometry for physical barriers widely adopted in countries such as Italy (e.g. Rolle *et al.*, 2009; Pedretti *et al.*, 2013b, 2017; Beretta, 2015). The total length of the barriers, $l_b$, was assumed to be three times the width of the sources ($l_b = 3W_S$). This was done to obtain a perfect lateral confinement of the source when simulating scenario "E" – i.e. the best configuration in terms of optimal pumping rates among those tested by B2004. The numerical implementation of the physical barriers in MODFLOW was done through the HFB package (Hsieh and Freckleton, 1993). The HFB package required a hydraulic conductivity $k_b$ and a thickness $X_b$ for the barriers, $k_b$. After initial tuning, we found $k_b = 10^{-7}$ m/d and $X_b = 0.5$m as a working combination of parameters limiting the advection across the barriers. For the 3D models, fully-penetrating barriers were assumed.

Operating within a MC framework, we adopted the first ($\overline{Q_n}$) and second ($\sigma_{Qn}^2$) moments of the ensemble of normalized optimal pumping rates to evaluate the MC results, and calculated from these moments coefficient of variation $CV$,

$$CV_{Qn} = \frac{\sqrt{\sigma_{Qn}^2}}{\overline{Q_n}}. \quad (5)$$

The coefficient of variation is a useful statistic for comparing the degree of variation from one data series to another, even if the means are drastically different from one another. For $CV_{Qn} \to 0$, the results suggest less uncertainty around the mean, while $CV_{Qn} \gg 0$ invalidates $\overline{Q_n}$, which becomes an aleatory outcome of the stochastic simulations.

Considering the two tested geostatistical models (SIS and SGS), the three tested P&T scenarios ("A","C" and "E") and the four tested multidimensional model setups ($N_L$=1, 10, 25 and 50), a total of 24 combinations of possible model setups were simulated in this work. While the original work by B2004 considered multiple correlation lengths and variances

per r.s.f. and 500 stochastic simulations per scenario, in this analysis it was decided to reduce the computational burden by focusing on a single correlation length ($I_Y = 25$), a single variance of $\sigma_Y^2 = 1.8$ and to 100 realizations per scenario. We performed a preliminary numerical test to evaluate whether the reduced amount of realizations used in this work was still sufficient to generate statistically valid results compared to the original work by Bayer et al. (2004). After calculating the confidence intervals of ensemble mean and variance by number of simulations (e.g. Ballio and Guadagnini, 2004), the results of this initial test suggested that 100 simulations were the minimum amount of simulations to obtain similar statistics as in the reference work by B2004 for the 2D scenario, which was used as a benchmark study. The resulting coefficient of variations were C$V$=0.07 for $\overline{Q_n}$ and CV= 0.08 for $\sigma_{Qn}^2$.

## 3.4 Geological entropy

Two metrics based on geological entropy were adopted in the analysis. The first metric was the entrogram scale (Bianchi and Pedretti, 2018), obtained after computing the entrogram of a r.s.f. In this work, the entrogram was coded in Matlab language and calculated in the following basic steps, as graphically described in Figure 2b and Figure 2c.

Firstly, the local entropy ($H_L$) is computed within a randomly-selected three-dimensional subdomain ($n_b$) in $\mathbb{R}^3$. The subdomain has dimension $\boldsymbol{l} = l_x\,\hat{\boldsymbol{\imath}} + l_y\,\hat{\boldsymbol{\jmath}} + l_z\,\hat{\boldsymbol{k}}$, where $\hat{\boldsymbol{\imath}}$, $\hat{\boldsymbol{\jmath}}$, $\hat{\boldsymbol{k}}$ are the unit vectors $\hat{\boldsymbol{\imath}}$=(1,0,0), $\hat{\boldsymbol{\jmath}}$ (1,0,0), $\hat{\boldsymbol{k}}$ (0,0,1) and $l_x, l_y$ and $l_z$ are the scalar components of $\boldsymbol{l}$, which is also termed the "entrogram lag". The $H_L$ is computed as

$$H_L(\boldsymbol{l}, n_b) = -\sum_{i=1}^{n_s} p_{L,i}(\boldsymbol{l}, n_b)[\ln p_{L,i}(\boldsymbol{l}, n_b)] \tag{6}$$

where $n_s$=10 is the total number of "hydrofacies" (i.e. the number of bins of the categorical $K$ pdf) and $p_{L,i}(\boldsymbol{l})$ are the local volumetric fractions (i.e., marginal probabilities of occurrence) of the categories within the subdomain. For $l_z \leq N_L$, the size of the subdomain is equal in all directions; for $l_z > N_L$, the maximum subdomain size in the vertical direction remain fixed to $N_L$ while $l_x, l_y$ increase (Figure 2b). The starting point of the random position of the subdomain is chosen using Matlab command `randperm`.

Second, the local entropy is normalized as

$$H'_R(\boldsymbol{l}, n_b) = \frac{H_L(\boldsymbol{l}, \_n_b)}{H_G} \tag{7}$$

where $H_G$ defines the entropy of the entire system. Third, (6) and (7) are repeated $N_B$ times, each time for a different, randomly-selected starting point, keeping the same subdomain size (Figure 2c). An average entropy is then computed as

$$H_R(\boldsymbol{l}) = \frac{1}{N_B} \sum_{n_b=1}^{\mathrm{N_B}} H'_R(\boldsymbol{l}, n_b) \tag{8}$$

After an initial sensitivity, we found $N_B = 100$ as a suitable working value. The operation (Equations 6-8) is then repeating over a range of lags, from smaller to larger values, and the results are plot by increasing lags to form the entrogram curve. In Bianchi and Pedretti (2018), the entrogram was used to evaluate the spatial persistency of the hydrofacies. In particular, the more persistent a hydrofacies is, the later the entrogram scales to $H_R = 1$. To quantify such persistency, Bianchi and Pedretti (2018) derived the entropic scale, $H_s$, as

$$H_s = \int_0^{\infty} [1 - H_R(l)] \mathrm{d}l \tag{9}$$

and concluded that systems characterized by larger $H_s$ tended to maintain longer correlation of the spatial order of the hydrofacies, and thus higher chances to generate preferential flow and solute channeling.

Another metric of interest to evaluate the spatial order of the system is the first-lag entrogram value, $H_{R0}$ , i.e. the value of the entrogram for $l_x, l_y, l_z = 1$. In Bianchi and Pedretti (2017), this metric was found to be well correlated to transport metrics defining the tendency of solute to experience preferential flow and channeled transport. Systems with lower $H_{R0}$ were more prone to show preferential flow and channeled transport than systems characterized by higher $H_{R0}$.

## 3.5 Dimensionless optimal pumping rates

Under homogeneous conditions for conventional P&T system, Javandel & Tsang (1986) developed an analytical formulation to optimize the well capture zones. Their solution suggested that the optimal pumping rate required to collect a contaminant with source width $W_S$ depended on the aquifer transmissivity $T$ and the gradient $i$. Accordingly, Bayer et al. (2004) introduced a dimensionless variable $Q_n$, which allowed comparing the results obtained from different model setup, including homogeneous and heterogeneous flow fields. The variable $Q_n$ was defined as

$$Q_n = \frac{Q_{opt}}{T_{eff} i W_s} \tag{10}$$

where $T_{eff}$=$K_{eff} b$. The parameter $K_{eff}$ is the effective hydraulic conductivity of the system, calculated numerically in this analysis as

$$K_{eff} = \frac{Q_{BC}}{L_Y L_z B i} \tag{11}$$

where $Q_{BC}$ is the volumetric discharge at the outflow boundary condition, calculated using the water budget tool (Harbaugh, 1990) coupled to MODFLOW-2000. In other words, $K_{eff}$ is the hydraulic conductivity that balances the groundwater outflow for a hydraulic gradient $i$ in presence of an active pumping well with rate $Q_{opt}$.

# 4 Results & Analysis

## 4.1 Optimal pumping rates

The main results from the analysis (mean $\overline{Q_n}$, variance $\sigma^2_{Qn}$ and coefficient of variation $CV_{Qn}$) are summarized in Table 2 for each combination of model parameters. The results are expressed both as actual values and as a percentage of the relative difference from the 2D model setup based on SGS, which served as a reference scenario to compare the other results.

A first important result is shown in Figure 3, which depicts the histograms of $Q_n$ obtained using SGS-based r.s.f. A visual inspection of the figure shows the distributions of $Q_n$ generated from the 2D models (left column) are generally shifted towards larger values compared to the 3D models with 50 layers (right column). For each model dimensionality, the distributions tend to be more shifted to higher values for scenario "A" (top row) than for scenario "C" (mid row) and "E" (bottom row). Comparing the combined P&T configurations, Scenario "E" seems to generate distributions with lower $Q_n$ than "C", and the difference is apparently more pronounced in 2D models than in 3D models.

This visual insight is quantitatively corroborated by the values reported in Table 2. The 2D model P&T setup "A" is the worst of the scenarios plotted in Figure 2. It provides the highest expected normalized optimal pumping rates ($\overline{Q_n}$ =1.624) and the largest uncertainty ($\sigma^2_{Qn}$ =0.917). Scenario "C" is the intermediate one ($\overline{Q_n}$ =1.303, $\sigma^2_{Qn}$ =0.623), while

scenario "E" provides the best setup minimizing both the expected pumping rates ($\overline{Q_n}$ = 0.706) and the uncertainty ($\sigma^2_{Qn}$=0.373). This result is consistent with and corroborates the conclusions by Bayer et al (2004), who also analyzed 2D SGS simulations.

The use of 3D models generated qualitative similar conclusions regarding the impact of physical barriers on the P&T efficiency. However, the calculated $\overline{Q_n}$ and $\sigma^2_{Qn}$ are different than in the 2D models, suggesting the specific values obtained from the stochastic simulations are strongly linked to the model dimensionality. In Figure 3 the histograms from the 50-layers models seem slightly shifted towards lower values compared to the 2D models. The variance is also reduced in 3D models than in 2D models. Table 2 corroborates and quantifies this visual insight. Compared to the 2D models, the 3D SGS models with 25 and 50 layers generate lower $\overline{Q_n}$, by 9-10% for Scenario "A" and by 64-66% for the Scenario "E" compared to the 2D scenarios. In terms of variance, the 3D SGS models with more than 25 layers generate a reduction in $\sigma^2_{Qn}$ of more than 97%.

A second important result is that the distribution of optimal pumping rates depends on the choice of the selected r.s.f. generator. Figure 4 depicts the cumulative density functions (cdfs) obtained from the ensemble of results from all simulated scenarios, by number of layers adopted in the models. Starting from the top-left panel, the case with $N_L = 1$ (i.e 2D simulations) shows that the cdfs from SIS-based models tend to shift the values towards higher pumping rates for all scenarios compared to SGS-based models. This is corroborated from Table 2, which shows that $\overline{Q_n}$ increases by 32% (Scenario "A"), 38% ("C") and 13% ("E") when passing from SGS to SIS. At the same time, the (uncertainty) also increases with SIS-based simulations, as $\sigma^2_{Qn}$ increases by 45% (Scenario "A"), 59% ("C") and 66% ("E") when passing from SGS to SIS.

For all scenarios we found $CV_{Qn} < 1$, which suggests that the results of the diverse realizations are close to the expected value in all simulated scenarios. It is interesting to note that Scenario "E" generates the highest coefficient of variations ($CV_{Qn} = 0.99$) of the entire combination of parameters tested in this work. This suggests a larger relative uncertainty in the results obtained from Scenario "E" configuration than in the results obtained from the other physical barrier configurations, even though Scenario "E" generates the lowest expected normalized pumping rates.

A graphical summary of the results presented in Table 2 is shown in Figure 5. Panel (a) shows the dependence of the mean pumping rates $\overline{Q_n}$ with the number of layers $N_L$, and panel (b) shows the correlation between the spread of the distributions $\sigma^2_{Qn}$ and $N_L$, by type of P&T configuration. The plots show a decreasing trend in $\overline{Q_n}$ and $\sigma^2_{Qn}$ for all P&T configurations as the number of layers increases. The decrease in variance is well correlated with $N_L$. The monotonicity of this correlation, independent from the type of stochastic generator, can be attributed to the fact that an increasing number of layers implies an increasing vertical mixing at the source. By keeping the same vertical correlation length of the hydraulic conductivity while adding layers means that the initial source size is increased, and so encompasses more heterogeneity. This aspect is further discussed in the following Section 5.

## 4.2 Geological entropy

Geological entropy metrics were used to elucidate the difference between model results. Figure 6 illustrates the entrograms of the r.s.f. by type of stochastic generator and number of layers. Figure 6a represents the normalized $H_R$ values over the lags, i.e. the distance between points used to calculate the entrogram, and essentially illustrates the persistence of the relative (normalized) geological entropy in space. The small inset (Figure 6b)

represents the non-normalized geological entropy. The maximum non-normalized value reached for each curve in the small inset (at lag 300) is the global geological entropy of the system ($H_G$).

A first highlighted aspect that emerges from the figure is that non-Gaussian simulations (SIS) tend to increase the spatial correlation of the relative geological entropy compared the curves of the Gaussian simulation (SGS), consistent with analysis by Bianchi and Pedretti (2018). The small inset (Figure 6b) also suggests that SGS generates a much higher global entropy $H_G$. This is explained considering that Gaussian r.s.f. show lower $H_G$ than SIS, as a consequence of the fact that Gaussian stochastic field generators tend to maximize spatial disorder through a minimization of the spatial continuity of extreme values (e.g. Journel and Deutsch, 1993). It results in shorter correlations of spatial ordering of $K$ clusters. Note that this is true because of the relatively small scale of the domain compared to the heterogeneity scales ($I_Y$), which causes statistically non-ergodic conditions. If the field and/or the number of simulations were much larger, $H_G$ should have been the same in all tested scenarios, given that the pdf of Y is identical in all simulations.

A second highlighted aspect is that the curves tend to scale according to the number of layers adopted in the simulations. In particular, we observe that simulations with lower $N_L$ tend to present higher spatial persistency of the relative entropy that simulations with higher $N_L$. This means that the simulations created by 2D models generate more spatial persistence of the order of $K$ clusters compared to 3D simulations. This result is novel, as no previous studies had systematically analyzed the role of $N_L$ in the scaling of the geological entropy metrics. The analysis is consistent with the conclusions by Bianchi and Pedretti (2018), who observed an increase in spatial correlation of the order of $K$ clusters when switching the models from 2D to 3D configurations. As discussed in the next section, in these simulations the vertical correlation length of the stochastic fields ($I_{Y(z)}$) remains constant

while the vertical domain size ($L_Z$) grows for increasing number of layers; as such, the dependency of the entrograms with $N_L$ can be a direct consequence of the different amount of heterogeneity sampled by the source for increasing $N_L$.

The insight from the visual analysis of Figure 6 are corroborated quantitatively in Figure 7, where the comparison between $N_L$ and the two metrics of geological entropy is illustrated. Figure 7a compares $N_L$ and the entrogram scale $H_S$. Here, we note that the SIS r.s.f. tend to generate higher $H_S$ than SGS r.s.f., reinforcing the idea that SIS-based models are expected to generate higher continuity of extreme patterns, which control the spatial order of $K$ clusters and in turn solute transport channeling, than SGS models. More specifically, for SGS r.s.f. the results seem to be independent from $N_L$ and ranging between $H_S$ =7.5-8. For SIS r.s.f the results range at higher values ($H_S = 12 - 16$) and are more correlated with $N_L$. An inverse linear correlation of form

$$N_L = -a_1 H_S + b_1 \tag{12}$$

where $a_1$=16.2 and $b_1$=62.0 was found to well describe the correlation (Pearson's coefficient $R^2 > 0.95$). For 2D models ($N_L = 0$), $H_S$ for SIS r.s.f. is about 2× than for SGS r.s.f, for 3D models with $N_L = 50$ the factor is about 1.5×, suggesting that the difference in spatial ordering is maximum for 2D models, consistent with the results presented above.

Figure 7b shows the correlation between $N_L$ and the first-lag relative entropy $H_{R0}$. We found that SIS-based models generate lower $H_{R0}$ than SGS-based models. This finding agrees with the inverse relationship between $H_S$ and $H_{R0}$ to describe the tendency of a system to generate solute channeling. We also observed that $H_{R0}$ is positively correlated with $N_L$ for SIS r.s.f. An exponential function of form

$$N_L = a_2 \exp(b_2 H_{R0}) \tag{13}$$

where $a_2 = 9.6 \times 10^{-3}$ and $b_2$=65.1 was found to well describe the correlation ($R^2$>0.95). The results reinforce the idea that 2D systems are more prone to generate solute channeling than 3D systems with increasing number of layers. The minimum value found for the 2D SIS r.s.f. ($H_{R0}$=0.07) is about 2.5× lower than the values found for 3D SGS r.s.f.

## 4.3 Discussion

The results from analysis suggest a dependence of the model layering and selected stochastic generator on the expected efficiency and uncertainty of the P&T systems. A first critical aspect to consider is that the stochastic simulations presented in this work adopted an isotropic correlation function with a fixed vertical integral scale, $I_{Y(z)} \approx 25$, while the vertical size of the domain ($L_Z$) is increased proportionally to the number of layers, $N_L$. By keeping $I_{Y(z)}$ constant, the ratio

$$I_Z = I_{Y(z)}/L_z \tag{14}$$

decreases as the number of layers increases, from $I_Z$ =25 for $N_L = 1$ to $I_Z$ =0.5 for $N_L$=50. The same number of particles is added to each additional layer of the system as $N_L$ increases, in such a way that adding layers means that the initial source size is increased encompassing (sampling) more heterogeneity. Observing Figure 5, it is likely that after 25 layers (i.e. $I_Z \approx 1$) the first two statistical moments of the normalized pumping rates ($\overline{Q_n}$ and $\sigma^2_{Qn}$) reached convergence for what refers to the level of system heterogeneity that is sampled considering the whole set of released solute plume. This is also in line with the marked drop of $\sigma^2_{Qn}$ for $N_L > 25$. The impact of the source size on solute transport evolution is well known in in stochastic hydrology (e.g. de Barros, 2018). For instance, previous analyses on radially convergent transport by Pedretti et al. (2013a, 2014) adopting 3D SGS simulations of conservative solutes showed that $I_Z$ had a strong influence on the formation of so-called

"anomalous" transport in heterogeneous media. Simulations with larger $I_Z$ resulted in longer BTC tailing and were more prone to show solute transport channeling along preferential flow zones rather than systems with lower ratios.

The results from the present work are well aligned with the results by Pedretti et al. (2013a, 2014) and the previous works on geological entropy. Notably, the well-defined correlation existing between $H_{R0}$ and $N_L$ (Figure 7) emphasizes the importance of the source size (measured by $I_Z$) and its effects of solute channeling. As described in detail in Bianchi and Pedretti (2017), $H_{R0}$ provides a statistical measure of the spatial order of the hydraulic conductivity among the smallest clusters of adjacent cells. This is true also for the cells corresponding to the source. As such, $H_{R0}$ can be seen as an indicator of spatial ordering of $K$ at the source. Since solute particles move preferentially along the most conductive parts of the aquifer, smaller $H_{R0}$ means that the solutes tend to move from the initial positions at the source to the adjacent cells (and from there to the rest of the domain) along the better-connected high-$K$ zones forming the solute channels. Higher $H_{R0}$, on the other hand, means that the system is more disordered, or in other terms more chaotic and better mixed. In this sense, the migration of the particles from the initial positions to the adjacent cells, and then to the rest of domain, is more similar in all parts of the injection zone. As such, the effect of channeling is reduced for systems with higher $H_{R0}$ than for systems lower $H_{R0}$.

Another related aspect with the importance of the adopted correlation lengths in these simulations is that the horizontal integral scale of the log-transformed hydraulic conductivity Y ($I_{Yh}$) is identical to the vertical integral scale of Y, $I_{Y(z)}$. Aquifers can be statistically anisotropic, with $I_{Yh} > I_{Y(z)}$ or $I_{Yh} < I_{Y(z)}$. For instance, in alluvial aquifers sandy-gravel bodies tend to be better correlated on the plane than in the vertical direction, due to sedimentary depositional processes (e.g. Kreitler, 1989; Scheibe and Freyberg, 1995; Koltermann and Gorelick, 1996). An opposite situation can be found in fractured aquifers

with vertically-oriented water-bearing fractures, as a consequence of other geological processes such as folding, faulting and deformation (e.g. Chilès, 2005; Dietrich, 2005; Pedretti et al., 2016, 2019). Corroborating if the results of a P&T optimization process are sensitive to selected anisotropy of the r.s.f. is left open for a future extension of the present analysis.

In this line, a potential limitation related to the use of the entrogram as computed in this work is that the subdomain $\boldsymbol{I}$, of size $l_x$, $l_y$ and $l_z$, becomes an rectangular box as the number of layers $N_L > l_z$. We are currently developing a more general anisotropic version of the entrogram, which should account for the different size in the model grid dimensions. We postulate that the use of an anisotropic entrogram will be particularly beneficial for the analysis of statistically anisotropic r.s.f. This hypothesis will be also tested in a future development of this work.

A further element to be analyzed in future extensions of the geological entropy includes the effects of hydromechanical dispersion. The present work was based purely on advective transport, as in the original work by Bayer et al. (2004). Recalling other studies on risk assessment (e.g. de Barros 2018), purely advective transport is usually adopted as a conservative approach for the decision-making process compared to the more physically based advective-dispersive transport. However, as in any other solute transport problems, the Péclet (Pe) number is expected to be an important parameter controlling the model outcomes. Pe→ 0 would increasingly smear the impact of $K$ heterogeneity, tending to enhance mixing among the streamtubes. We postulate that all particles BTCs would look more alike, tending to a more statistically homogeneous transport even for low $H_{R0}$ or large $H_S$. So, potentially the uncertainty around the mean values could reduce for low Pe. These aspects shall be tested through a sound and rigorous sensitivity analyses targeting a range of Pe values.

# Summary and conclusion

The cost-effective design and use of P&T require minimizing the overall pumping rates from the hydraulic barrier, a task plagued with uncertainty due to geological heterogeneity. Our stochastic modeling analyses extended the conclusion of previous works, particularly Bayer et al. (2004), evaluating the implication of model dimensionality and the selected geostatistical random spatial field (r.s.f.) generator on the expected optimal pumping rates ($Q_{opt}$) and the uncertainty depending on different conventional and combined P&T configurations.

There are three main conclusions from this work.

1) The results of the P&T optimization process based on stochastic numerical modeling depends strictly on the selected model dimensionality. Using a 2D model, the expected behavior of the system (measured by the ensemble mean of normalized optimal pumping rates, $\overline{Q_n}$) and the uncertainty (measured by the ensemble-mean variance $\sigma^2_{Qn}$) are maximized compared to 3D models, for the same adopted r.s.f generator. This could be linked to the relative amount of heterogeneity sampled by the source related to the vertical size of the domain, which can be measured by $I_Z = I_{Y(z)}/L_z$. As $N_L$ increases, $I_Z$ is lower and the expected pumping rates tend to be reduced in all P&T configurations, particularly for scenario "E", where we found a decrease up to 67% for the model embedding $N_L = 50$ compared to the 2D model. The uncertainty also tends to decrease for growing $N_L$, with reduction up to 99% in $\sigma^2_{Qn}$ for certain P&T configurations, as a consequence of the fact that the source is better mixed for lower $I_Z$.

2) The results of the P&T optimization process depend strictly on the selected stochastic field generator. Non-Gaussian (SIS) simulations determine a generalized increase in $\overline{Q_n}$ and $\sigma^2_{Qn}$ compared to Gaussian (SGS) simulations. The use of 3D modeling does not help to reduce the departures between SGS and SIS compared to the 2D modeling; in some cases, a higher number of layers may even generate higher expected optimal pumping rates. The uncertainty around the mean also increased when using SIS-based modeling compared to SGS-based modeling. The use of combined P&T configurations, in particular Scenario "E", was observed to be useful for both SGS and SIS simulations.

3) Geological entropy can explain the different distributions of optimal pumping rates. We found that 2D models and SIS-based models tend to be characterized by lower $H_{R0}$ and higher $H_S$ than 3D models and SGS-based models. This is particularly true when increasing the discretization of 3D models along the vertical direction, i.e. increasing $N_L$ and reducing in turn $I_Z$. The higher mean pumping rates and uncertainty in 2D and SIS models can be thus explained considering that systems with lower $H_{R0}$ and higher $H_s$ tend to be more prone to solute transport channeling (Bianchi and Pedretti, 2017, 2018), which are consistent with the effect of $I_Z$ at the source evaluated in previous works on radial convergent transport in 3D heterogeneous systems (Pedretti *et al.*, 2013a, 2014). As $\overline{Q_n}$ and $\sigma^2_{Qn}$ depend strictly on the amount of preferential flow and solute channeling in the system (e.g. Bayer *et al.*, 2004; Bayer and Finkel, 2006), systems showing lower persistency of spatial order on $K$ clusters are more homogeneous ("well-mixed") and generate less spatial variability in solute patterns, thus requiring less pumping rates (lower Q) to collect all particles, than systems characterize by higher spatial persistency of $K$ clusters.

Accepted ms, GEM International Journal on Geomathematics doi:10.1007/s13137-020-00158-8

# Acknowledgements

The author acknowledges two anonymous reviewers whose comments raised the quality of this paper, and Dr Marco Bianchi for the initial discussion on the manuscript content. All data generated from this work, including algorithms to run the stochastic fields and the MC simulations, can be requested to the author.

Accepted ms, GEM International Journal on Geomathematics doi:10.1007/s13137-020-00158-8

# Tables

Table 1 Key input parameters of the model setup used in this study.

| Description | Symbol | Value | Units |
|---|---|---|---|
| Height of contaminant source | $H_s$ | 50 | m |
| Width of contaminant source | $W_s$ | 50 | m |
| Distance of the source from the pumping well | $r$ | 50 | m |
| Total length of the physical barrier | $l_b$ | 150 | m |
| Effective aquifer transmissivity | $T_{eff}$ | variable | $m^2/d$ |
| Mean aquifer gradient | $i$ | 0.001 | - |
| Integral scale of log-transformed hydraulic conductivity | $I_Y$ | 25 | m |
| Variance of log-transformed hydraulic conductivity | $\sigma_Y^2$ | 1.8 | - |

Table 2 Resulting ensemble mean ($\overline{Q_n}$) and variance ($\sigma^2_{Qn}$) of the normalized optimal pumping rates by scenario. SGS/SIS refers to the type of stochastic simulator; $N_L$ is the number of layers. For each case, the next line represents the relative increment (as percentage) relatively to the case "SGS - $N_L$=1"

| | P&T configuration "A" | | | | | | | |
|---|---|---|---|---|---|---|---|---|
| $N_L$ | 1 | | 10 | | 25 | | 50 | |
| SGS/SIS | SGS | SIS | SGS | SIS | SGS | SIS | SGS | SIS |
| $\overline{Q_n}$ | 1.624 | 2.142 | 1.835 | 2.173 | 1.479 | 1.683 | 1.467 | 1.668 |
| | - | 32% | 13% | 34% | -9% | 4% | -10% | 3% |
| $\sigma^2_{Qn}$ | 0.917 | 1.334 | 0.478 | 1.218 | 0.029 | 0.107 | 0.025 | 0.112 |
| | - | 45% | -48% | 33% | -97% | -88% | -97% | -88% |
| $CV_{Q_n}$ | 0.59 | 0.54 | 0.38 | 0.51 | 0.11 | 0.19 | 0.11 | 0.20 |
| | - | -9% | -36% | -14% | -81% | -67% | -82% | -66% |
| | P&T configuration "C" | | | | | | | |
| $N_L$ | 1 | | 10 | | 25 | | 50 | |
| SGS/SIS | SGS | SIS | SGS | SIS | SGS | SIS | SGS | SIS |
| $\overline{Q_n}$ | 1.303 | 1.803 | 1.382 | 1.682 | 0.863 | 1.170 | 0.840 | 1.146 |
| | - | 38% | 6% | 29% | -34% | -10% | -36% | -12% |
| $\sigma^2_{Qn}$ | 0.623 | 0.988 | 0.331 | 0.522 | 0.021 | 0.130 | 0.017 | 0.141 |
| | - | 59% | -47% | -16% | -97% | -79% | -97% | -77% |
| $CV_{Q_n}$ | 0.606 | 0.551 | 0.417 | 0.429 | 0.170 | 0.308 | 0.156 | 0.328 |
| | | -9% | -31% | -29% | -72% | -49% | -74% | -46% |
| | P&T configuration "E" | | | | | | | |
| $N_L$ | 1 | | 10 | | 25 | | 50 | |
| SGS/SIS | SGS | SIS | SGS | SIS | SGS | SIS | SGS | SIS |
| $\overline{Q_n}$ | 0.706 | 0.798 | 0.493 | 0.712 | 0.252 | 0.347 | 0.241 | 0.232 |
| | - | 13% | -30% | 1% | -64% | -51% | -66% | -67% |
| $\sigma^2_{Qn}$ | 0.373 | 0.620 | 0.089 | 0.268 | 0.004 | 0.021 | 0.007 | 0.026 |
| | - | 66% | -76% | -28% | -99% | -94% | -98% | -93% |
| $CV_{Q_n}$ | 0.87 | 0.99 | 0.61 | 0.73 | 0.24 | 0.42 | 0.35 | 0.70 |
| | | 14% | -30% | -16% | -72% | -52% | -60% | -20% |

# Figures

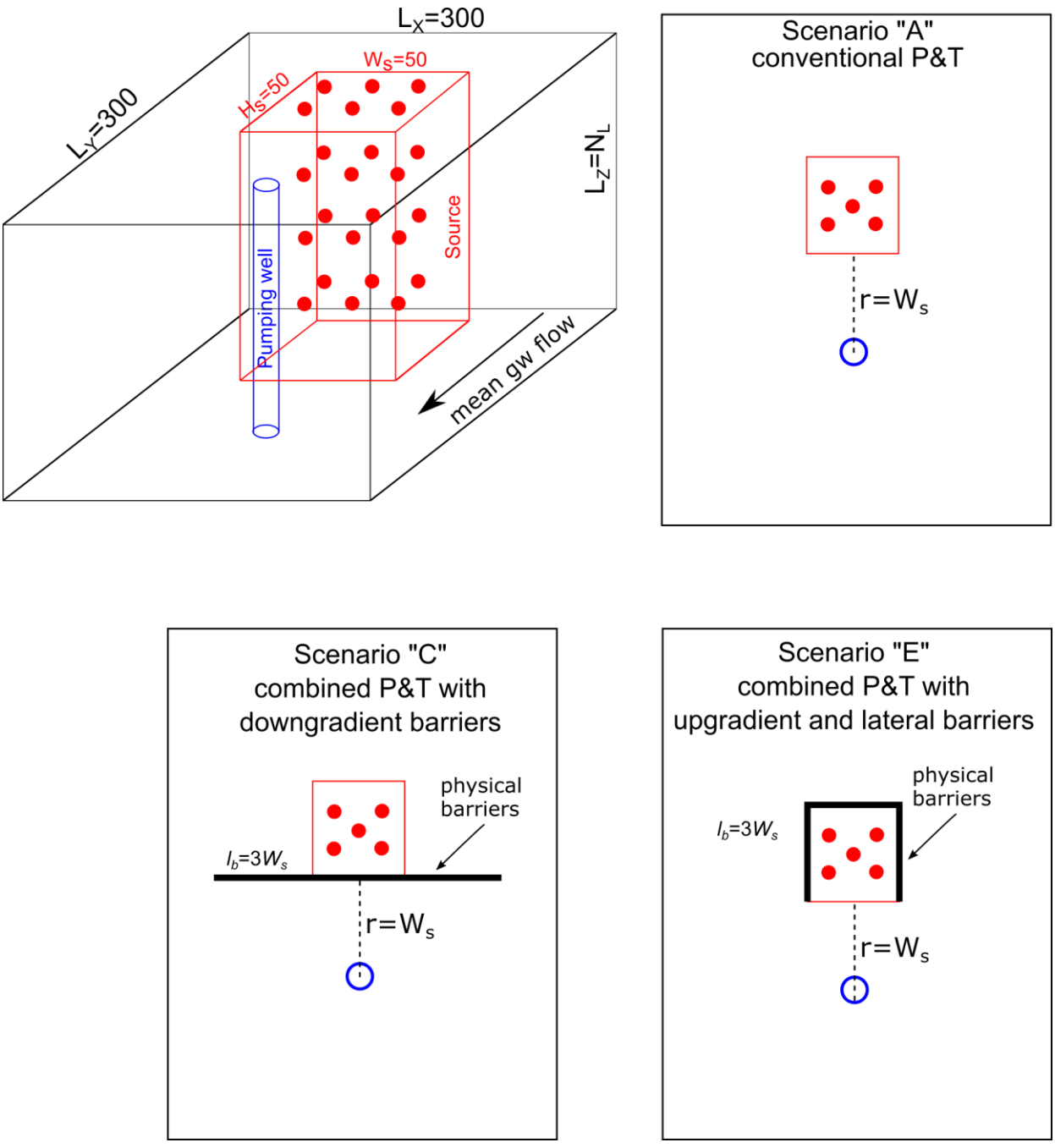


Figure 1 The top left panel illustrates the 3D conceptual models and boundary conditions adopted in the models. The mass in the source area (red), of size $W_s \times H_s = 50 \times 50$, is discretized in $N_p$=200 particles per layer. The other plots represent the bird-view of the system. In all scenarios, the distance of the pumping well (blue) from the bottom edge of the source is equal to the lateral extension of the source ($r = W_S$). For the combined scenarios "C" and "E", the total length of the physical barrier is equal to three times the lateral extension of the source ($l_b = 3W_S$).

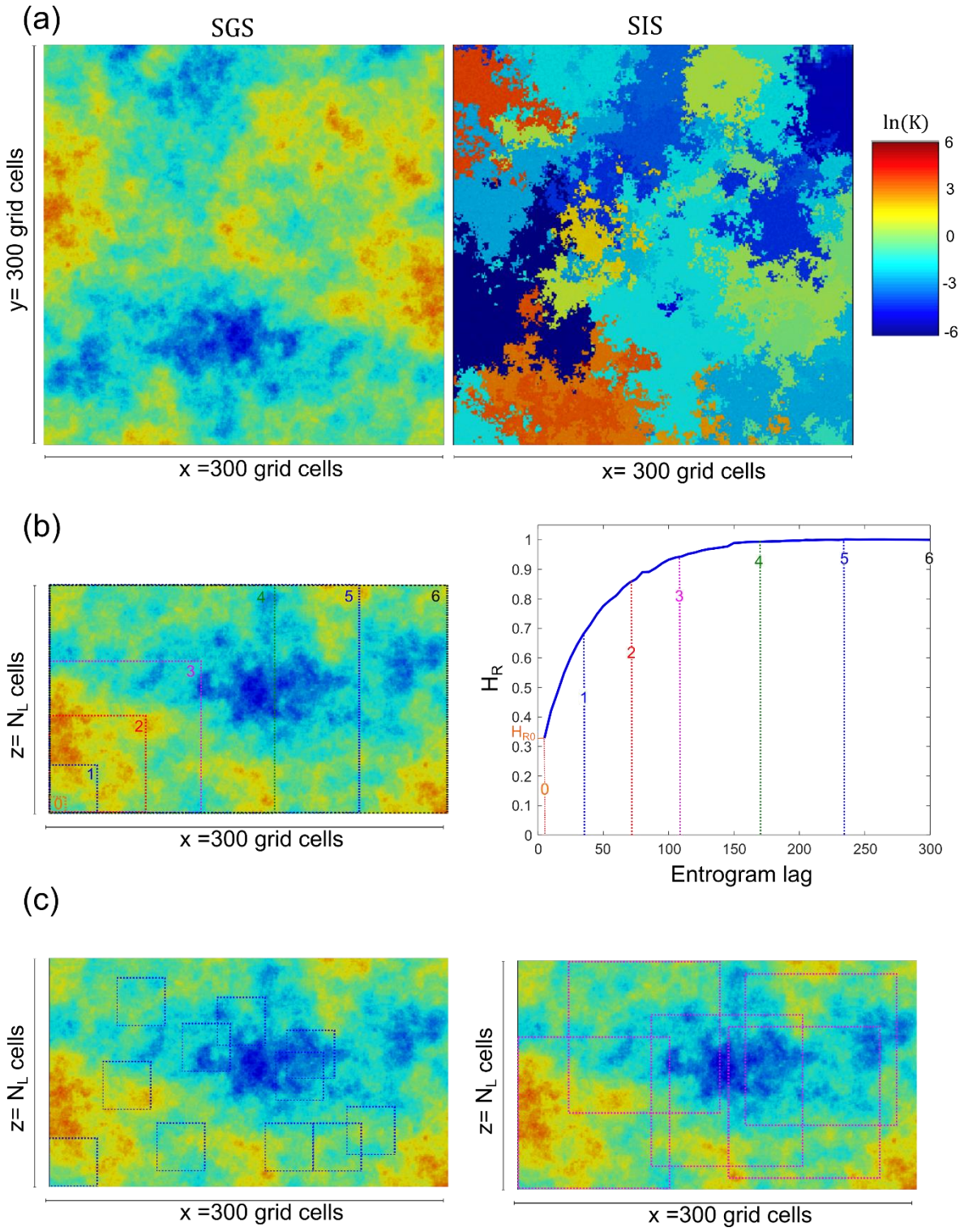


Figure 2 (a) Planar views of two random realizations created using the SGS (left) and SIS (right) methods. (b) Increasing size (lag) of the subdomains (left) used to compute the entrogram (right). The entrogram shows the relative entropy ($H_R$) against the entrogram lag; $H_{R0}$ refers to the smallest subdomain used to calculate $H_R$. (c) Randomly selected subdomains of two different scales used to compute the entrogram.

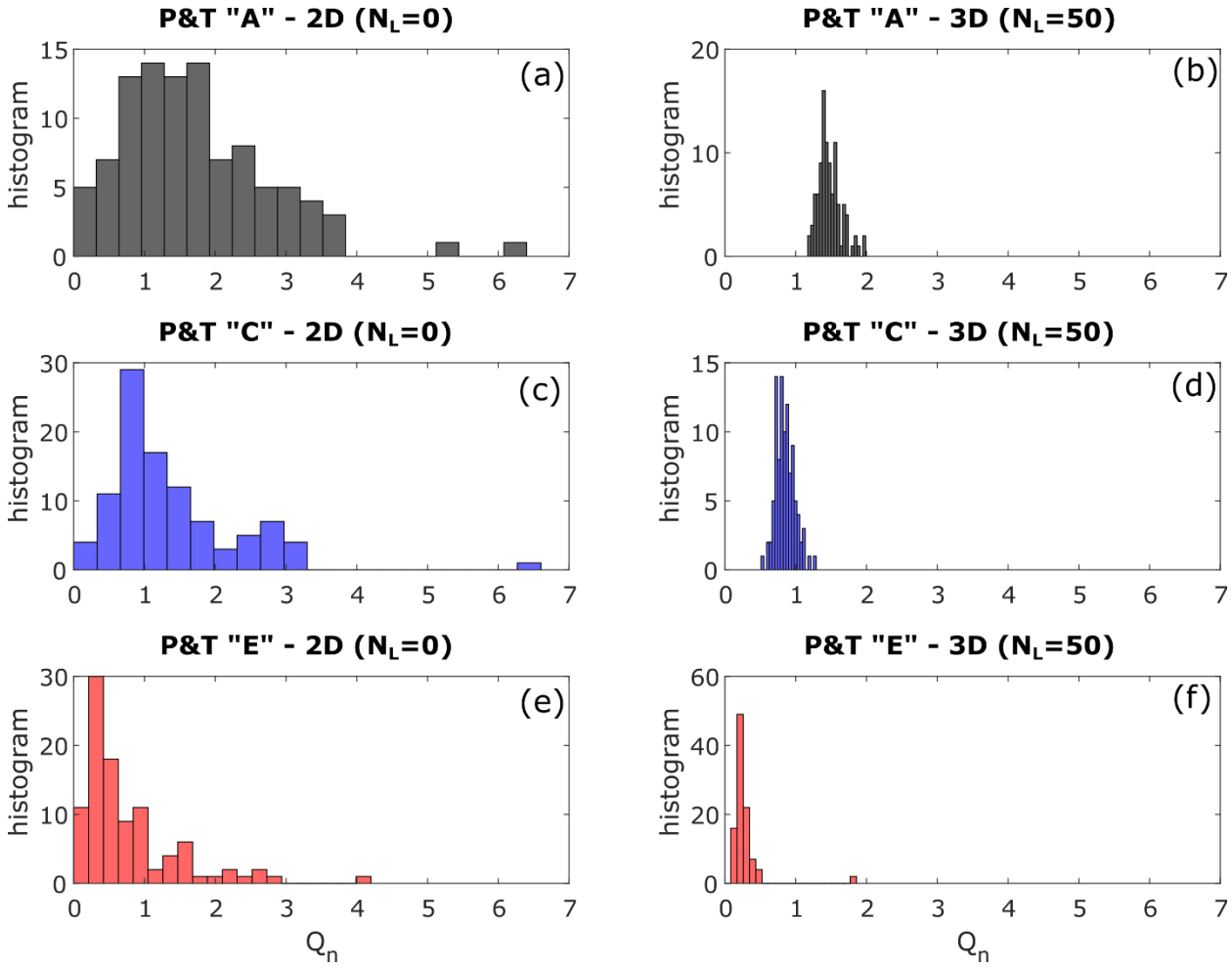


Figure 3 Histograms of the ensemble of the resulting optimal pumping rates ($Q_n$, unitless) for each of P&T scenario "A" – conventional P&T with no physical barriers; "C": combined P&T with downgradient barriers; "E" – combined P&T with upgradient and lateral barrier) by number of layers ($N_L$). The results refer to the Sequential Gaussian Simulations (SGS).

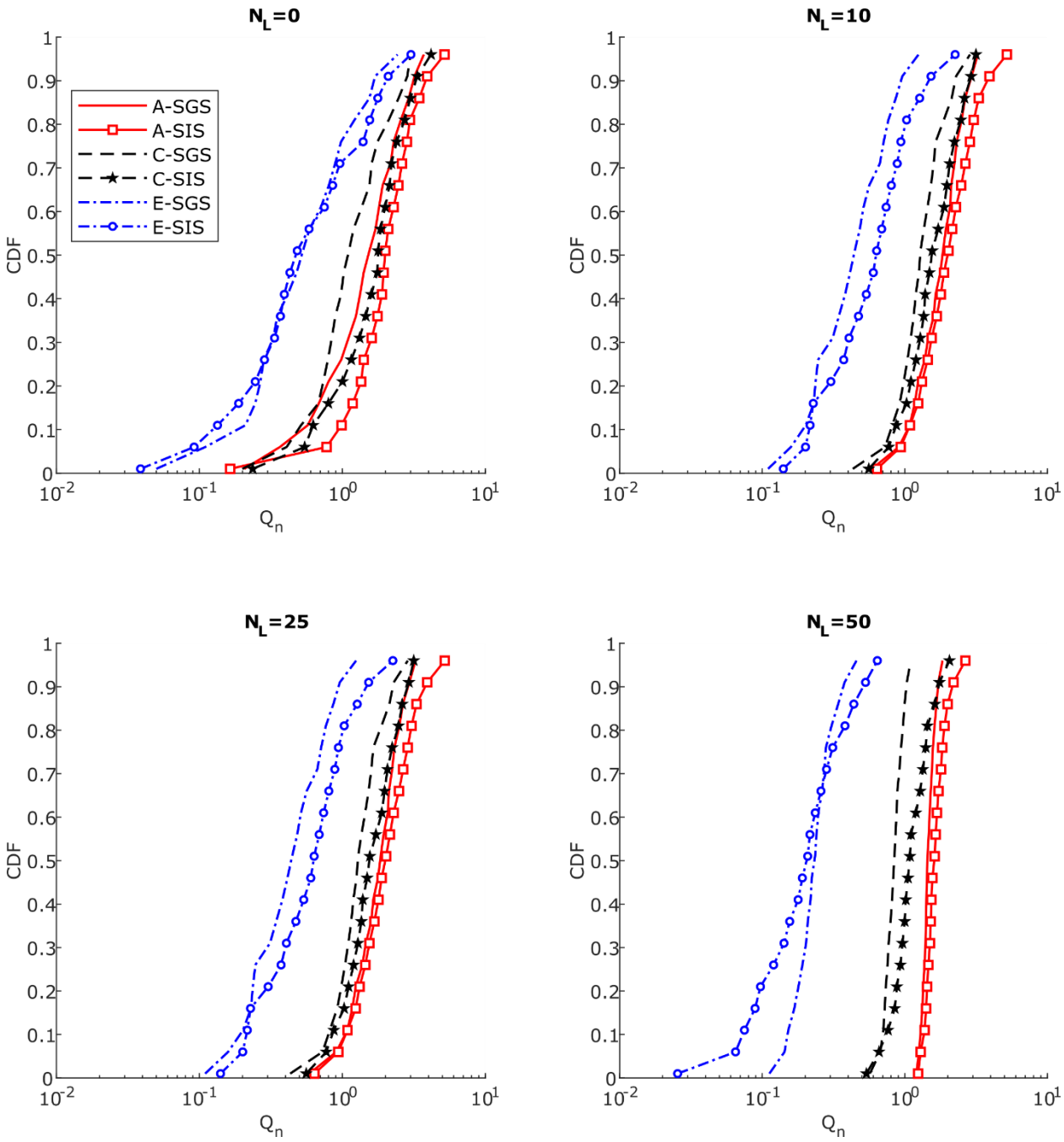


Figure 4 Cumulative density functions (cdfs) of the resulting optimal pumping rates ($Q_n$) for each of P&T scenario ("A","C","E"), by number of layers ($N_L$) and type of random field generator (SGS=Sequential Gaussian Simulation; SIS= Sequential Indicator Simulation).

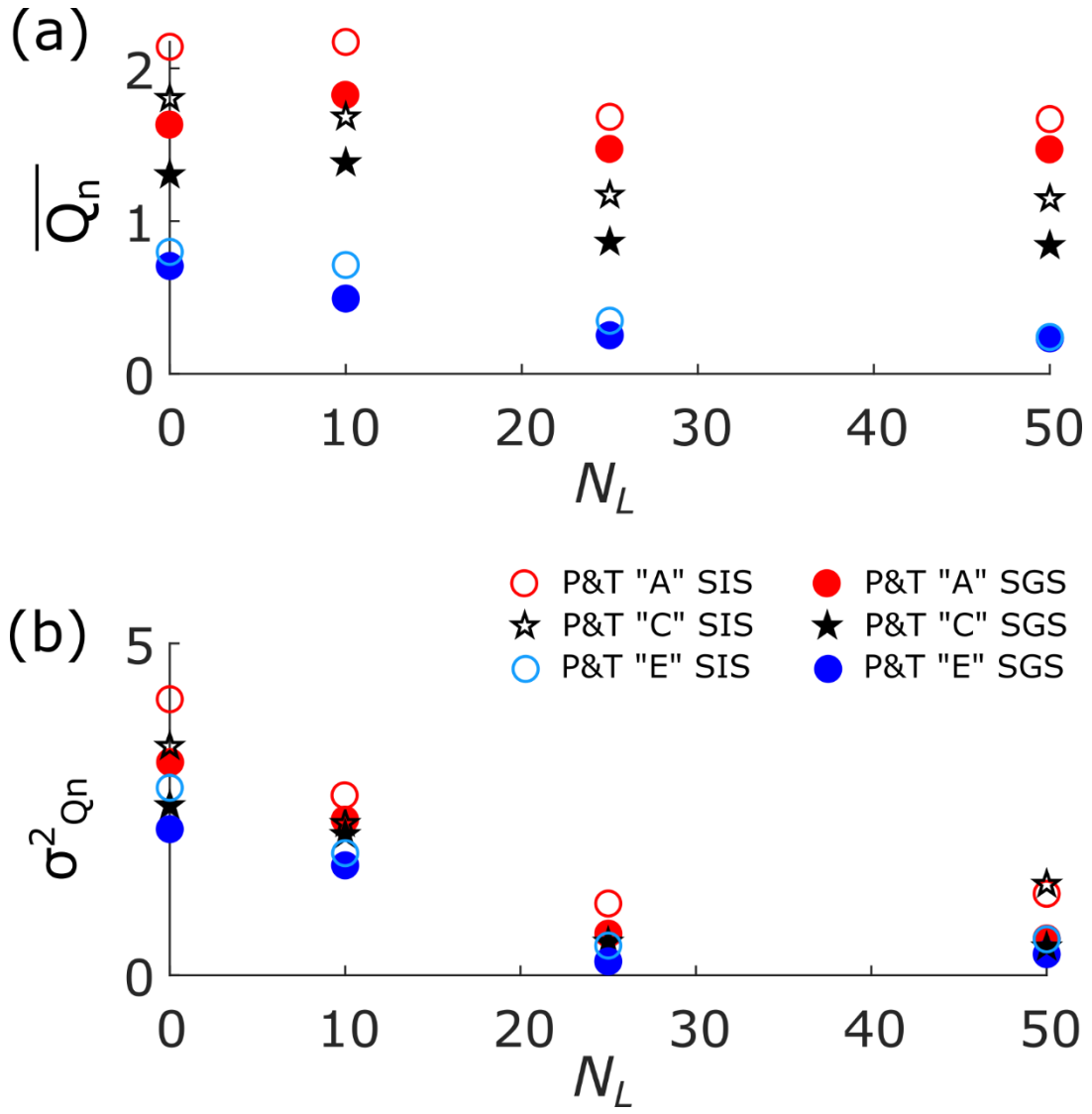


Figure 5 Ensemble-mean (a) and variance (b) of the optimal normalized pumping rates by number of layers, type of stochastic simulator and type of P&T setup.

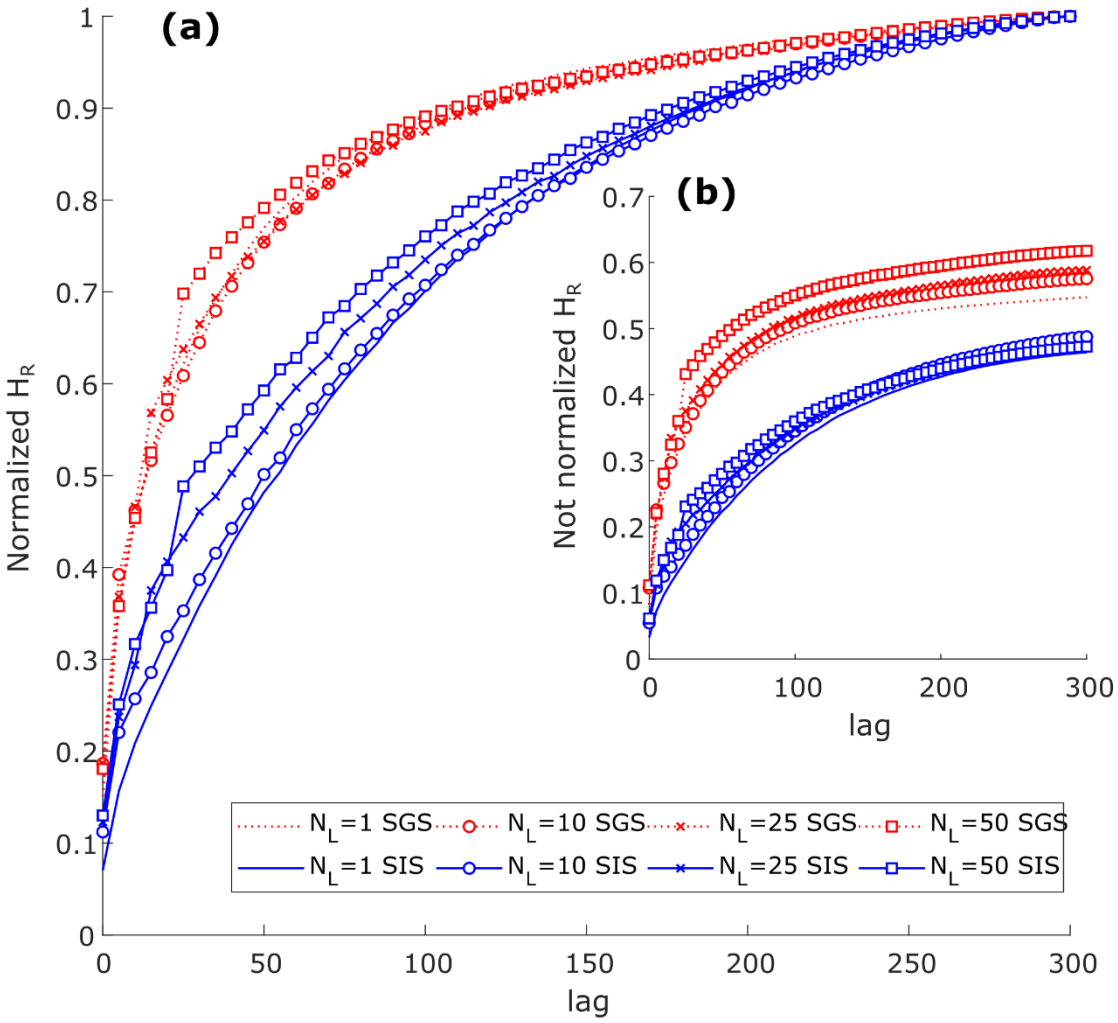


Figure 6 Entrograms for the different geological setups. Note that all setups involve the same exponential variogram (integral scale $I$=1.53) and variance of the log-transformed hydraulic conductivity ($\sigma_Y^2 = 1.8$), by number of layers ($N_L$) and type of random field generator (SGS=Sequential Gaussian Simulation; SIS= Sequential Indicator Simulation) used in the simulations. The larger plot (a) illustrates the normalized (relative) geological entropy ($H_R$), the smaller inset (b) shows the local geological entropy ($H_L$).

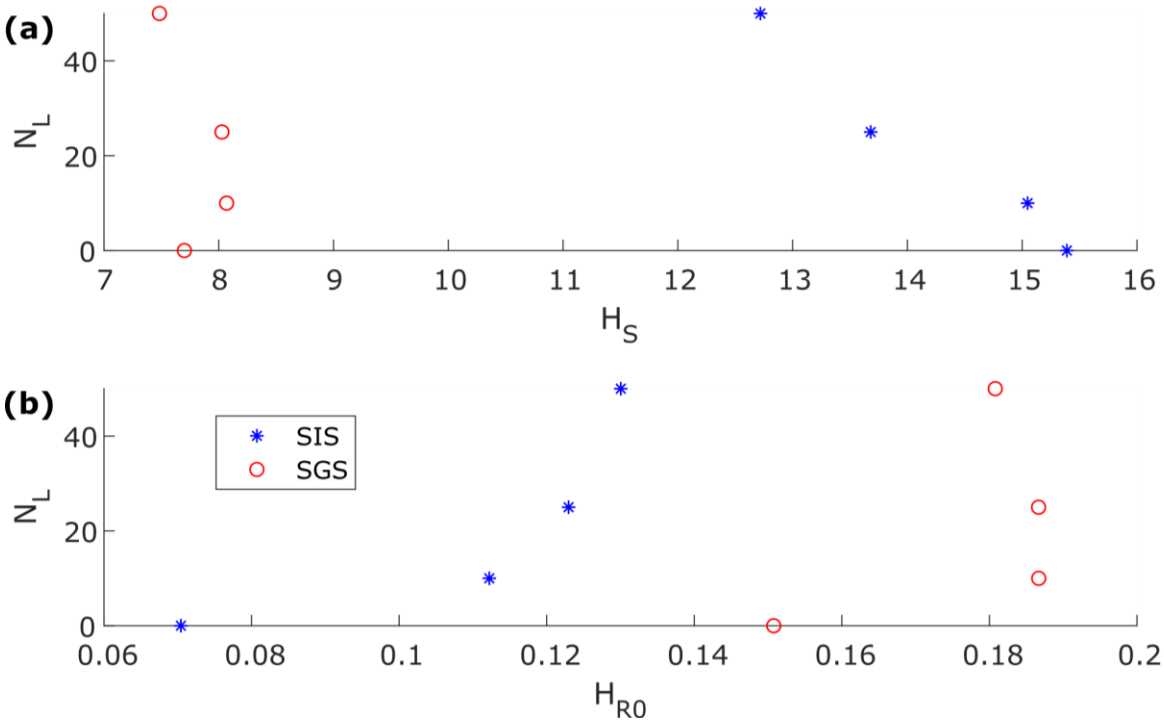


Figure 7 Comparison between number of layers ($N_L$) and metrics based on the geological entropy, by type of stochastic generator. On top (a), the metric is the entrogram scale ($H_S$). At the bottom (b), the metric is the first-lag normalized relative entropy ($H_{R0}$)

# References

Ballio F, Guadagnini A. 2004. Convergence assessment of numerical Monte Carlo simulations in groundwater hydrology. *Water Resources Research*. John Wiley & Sons, Ltd, 40(4). https://doi.org/10.1029/2003WR002876.

Bayer P, Finkel M. 2006. Conventional and Combined Pump-and-Treat Systems Under Nonuniform Background Flow. *Groundwater*, 44(2): 234–243. https://doi.org/10.1111/j.1745-6584.2005.00191.x.

Bayer P, Finkel M, Teutsch G. 2004. Combining Pump-and-Treat and Physical Barriers for Contaminant Plume Control. *Ground Water*, 42(6): 856–867. https://doi.org/10.1111/j.1745-6584.2004.t01-4-.x.

Bayer P, Finkel M, Teutsch G. 2005. Cost-optimal contaminant plume management with a combination of pump-and-treat and physical barrier systems. *Groundwater Monitoring & Remediation*, 25(2): 96–106. https://doi.org/10.1111/j.1745-6592.2005.0022.x.

Beretta GP. 2015. Some aspects of the state of the art of contaminated sites remediation in Italy. *Acque Sotterranee - Italian Journal of Groundwater*, 4(2). https://doi.org/10.7343/as-107-15-0134.

Berkowitz B, Balberg I. 1993. Percolation theory and its application to groundwater hydrology. *Water Resources Research*, 29(4): 775–794. https://doi.org/10.1029/92WR02707.

Bianchi M, Kearsey T, Kingdon A. 2015. Integrating deterministic lithostratigraphic models in stochastic realizations of subsurface heterogeneity. Impact on predictions of lithology, hydraulic heads and groundwater fluxes. *Journal of Hydrology*, 531: 557–573. https://doi.org/10.1016/j.jhydrol.2015.10.072.

Bianchi M, Pedretti D. 2017. Geological entropy and solute transport in heterogeneous porous media. *Water Resources Research*, 53(6): 4691–4708. https://doi.org/10.1002/2016WR020195.

Bianchi M, Pedretti D. 2018. An Entrogram-Based Approach to Describe Spatial Heterogeneity With Applications to Solute Transport in Porous Media. *Water Resources Research*, 54(7): 4432–4448. https://doi.org/10.1029/2018WR022827.

Carle SF, Fogg GE. 1997. Modeling Spatial Variability with One and Multidimensional Continuous-Lag Markov Chains. *Mathematical Geology*, 29(7): 891–918. https://doi.org/10.1023/A:1022303706942.

Casasso A, Tosco T, Bianco C, Bucci A, Sethi R. 2020. How Can We Make Pump and Treat Systems More Energetically Sustainable? *Water*, 12(1): 67. https://doi.org/10.3390/w12010067.

Chilès J-P. 2005. Stochastic Modeling of Natural Fractured Media: A Review. In: Leuangthong O and Deutsch CV (eds) *Geostatistics Banff 2004*. Springer Netherlands: Dordrecht, 285–294.

Dagan G. 1989. Flow and transport in porous formations. , xvii + 465 pp.

de Barros FPJ. 2018. Evaluating the combined effects of source zone mass release rates and aquifer heterogeneity on solute discharge uncertainty. *Advances in Water Resources*, 117: 140–150. https://doi.org/10.1016/j.advwatres.2018.05.010.

Deutsch C, Journel A. 1998. *GSLIB: Geostatistical Software Library and User's Guide*. Oxford University Press, New York, 340 p.

Dietrich P (ed). 2005. *Flow and transport in fractured porous media*. Springer: Berlin ; New York.

Dominijanni A, Manassero M, Boffa G, Puma S. 2017. Intrinsic and State Parameters Governing the Efficiency of Bentonite Barriers for Contaminant Control. In: Ferrari A and Laloui L (eds) *Advances in Laboratory Testing and Modelling of Soils and Shales (ATMSS)*. Springer International Publishing, 45–56.

Emery X. 2004. Properties and limitations of sequential indicator simulation. *Stochastic Environmental Research and Risk Assessment*, 18(6): 414–424. https://doi.org/10.1007/s00477-004-0213-5.

EPA. 2005. Cost-Effective Design of Pump and Treat Systems. , 38.

Fernàndez-Garcia D, Illangasekare TH, Rajaram H. 2005. Differences in the scale-dependence of dispersivity estimated from temporal and spatial moments in chemically and physically heterogeneous porous media. *Advances in Water Resources*, 28(7): 745–759. https://doi.org/10.1016/j.advwatres.2004.12.011.

Fiori A, Jankovic I. 2012. On Preferential Flow, Channeling and Connectivity in Heterogeneous Porous Formations. *Mathematical Geosciences*, 44(2): 133–145. https://doi.org/10.1007/s11004-011-9365-2.

Freeze RA. 1975. A stochastic-conceptual analysis of one-dimensional groundwater flow in nonuniform homogeneous media. *Water Resources Research*, 11(5): 725–741. https://doi.org/10.1029/WR011i005p00725.

Freeze RA. 2004. The role of stochastic hydrogeological modeling in real-world engineering applications. *Stochastic Environmental Research and Risk Assessment*, 18(4): 286–289.

Gómez-Hernandez JJ, Wen X-H. 1998. To be or not to be multi-Gaussian? A reflection on stochastic hydrogeology. *Advances in Water Resources*, 21(1): 47–61. https://doi.org/10.1016/S0309-1708(96)00031-0.

Harbaugh AW. 1990. *A computer program for calculating subregional water budgets using results from the US Geological Survey modular three-dimensional finite-difference ground-water flow model*. .

Harbaugh AW, Banta ER, Hill MC, McDonald MG. 2000. *MODFLOW-2000, the U.S. Geological Survey modular ground-water model – User guide to modularization concepts and the Ground-Water Flow Process*. U.S. Geological Survey Open-File Report 00-92, 121 p.

Hsieh PA, Freckleton JR. 1993. *Documentation of a computer program to simulate horizontal-flow barriers using the US Geological Survey's modular three-dimensional finite-difference ground-water flow model*. US Geological Survey.

Huang L, Ritzi RW, Ramanathan R. 2012. Conservative Models: Parametric Entropy vs. Temporal Entropy in Outcomes. *Groundwater*, 50(2): 199–206. https://doi.org/10.1111/j.1745-6584.2011.00832.x.

Javandel I, Tsang C-F. 1986. Capture-Zone Type Curves: A Tool for Aquifer Cleanup. *Groundwater*, 24(5): 616–625. https://doi.org/10.1111/j.1745-6584.1986.tb03710.x.

Journel AG, Deutsch CV. 1993. Entropy and spatial disorder. *Mathematical Geology*, 25(3): 329–355. https://doi.org/10.1007/BF00901422.

Koltermann CE, Gorelick S. 1996. Heterogeneity in sedimentary deposits: A review of structure-imitating, process-imitating, and descriptive approaches. *Water Resources Research*, 32(9): 2617–2658.

Kreitler CW. 1989. Hydrogeology of sedimentary basins. *Journal of Hydrology*, 106(1–2): 29–53. https://doi.org/10.1016/0022-1694(89)90165-0.

Kuppusamy S, Palanisami T, Megharaj M, Venkateswarlu K, Naidu R. 2016. In-Situ Remediation Approaches for the Management of Contaminated Sites: A Comprehensive Overview. In: de Voogt P (ed) *Reviews of Environmental Contamination and Toxicology Volume 236*. Springer International Publishing: Cham, 1–115.

Mackay DM, Cherry JA. 1989. Groundwater contamination: pump-and-treat remediation. *Environmental Science & Technology*, 23(6): 630–636. https://doi.org/10.1021/es00064a001.

Mays DC, Faybishenko BA, Finsterle S. 2002. Information entropy to measure temporal and spatial complexity of unsaturated flow in heterogeneous media. *Water Resources Research*, 38(12). https://doi.org/10.1029/2001WR001185.

McDonald MG, Harbaugh AW. 1988. *A modular three-dimensional finite-difference ground-water flow model*. US Geological Survey.

Pedretti D, Bianchi M. 2019. Preliminary results from the use of entrograms to describe transport in fractured media. *Acque Sotterranee - Italian Journal of Groundwater*. https://doi.org/10.7343/as-2019-421.

Pedretti D, Fernàndez-Garcia D, Bolster D, Sanchez-Vila X. 2013a. On the formation of breakthrough curves tailing during convergent flow tracer tests in three-dimensional heterogeneous aquifers. *Water Resources Research*, 49(7): 4157–4173. https://doi.org/10.1002/wrcr.20330.

Pedretti D, Fernàndez-Garcia D, Sanchez-Vila X, Bolster D, Benson DA. 2014. Apparent directional mass-transfer capacity coefficients in three-dimensional anisotropic heterogeneous aquifers under radial convergent transport. *Water Resources Research*, 50(2): 1205–1224. https://doi.org/10.1002/2013WR014578.

Pedretti D, Luoma S, Ruskeeniemi T, Backman B. 2019. A geologically-based approach to map arsenic risk in crystalline aquifers: Analysis of the Tampere region, Finland. *Geoscience Frontiers*. https://doi.org/10.1016/j.gsf.2018.12.004.

Pedretti D, Marco Masetti, Giovanni P. Beretta, Mariangela Vitiello. 2013b. A Revised Conceptual Model to Reproduce the Distribution of Chlorinated Solvents in the Rho Aquifer (Italy). *Groundwater Monitoring & Remediation*, 33(3): 69–77. https://doi.org/10.1111/gwmr.12017.

Pedretti D, Masetti M, Beretta GP. 2017. Stochastic analysis of the efficiency of coupled hydraulic-physical barriers to contain solute plumes in highly heterogeneous aquifers. *Journal of Hydrology*, 553(Supplement C): 805–815. https://doi.org/10.1016/j.jhydrol.2017.08.051.

Pedretti D, Mayer U, Beckie RD. 2020. Controls of uncertainty in acid rock drainage predictions from waste rock piles examined through Monte-Carlo multicomponent reactive transport. *Stochastic Environmental Research and Risk Assessment*, In press. https://doi.org/10.1007/s00477-019-01756-1.

Pedretti D, Russian A, Sanchez-Vila X, Dentz M. 2016. Scale dependence of the hydraulic properties of a fractured aquifer estimated using transfer functions. *Water Resources Research*, 52(7): 5008–5024. https://doi.org/10.1002/2016WR018660.

Pham TD. 2010. GeoEntropy: A measure of complexity and similarity. *Pattern Recognition*, 43(3): 887–896. https://doi.org/10.1016/j.patcog.2009.08.015.

Pham TD, Yan H. 2018. Spatial-dependence recurrence sample entropy. *Physica A: Statistical Mechanics and its Applications*, 494: 581–590. https://doi.org/10.1016/j.physa.2017.12.015.

Pollock DW. 1994. *User's Guide for: MODPATH/MODPATH-PLOT, Version 3: A particle tracking post-processing package for MODFLOW, the U.S. Geological Survey finite-difference ground-water flow model, Documentation of MODPATH*. U.S. Geological Survey Open-File Report 94-464, 6 ch.

Remy N, Boucher A, Wu J. 2009. *Applied Geostatistics with SGeMS. A User's Guide*. .

Rolle E, Beretta GP, Majone M, Pedretti D, Petrangeli Papini M, Raffaelli L. 2009. Analisi delle alternative tecnologiche per il contenimento della contaminazione di acque sotterranee. paper presented at the Reindustrializzazione di siti industriali inquinati e tecnologie di intervento sulle acque sotterranee e sui sedimenti. Ministry of Economic Development, Rome, Italy.

Rubin Y, Cushey MA, Bellin A. 1994. Modeling of transport in groundwater for environmental risk assessment. *Stochastic Hydrology and Hydraulics*, 8(1): 57–77. https://doi.org/10.1007/BF01581390.

Sanchez-Vila X, Guadagnini A, Carrera J. 2006. Representative hydraulic conductivities in saturated groundwater flow. *Reviews of Geophysics*, 44(3). https://doi.org/10.1029/2005RG000169.

Sartore L, Fabbri P, Gaetan C. 2016. spMC: an R-package for 3D lithological reconstructions based on spatial Markov chains. *Computers & Geosciences*, 94: 40–47. https://doi.org/10.1016/j.cageo.2016.06.001.

Scheibe T. 1993. Characterization of the spatial structuring of natural porous media and its impacts on subsurface flow and transport. PhD Thesis, Stanford, US, Stanford University.

Scheibe TD, Freyberg DL. 1995. Use of sedimentological information for geometric simulation of natural porous media structure. *Water Resources Research*, 31(12): 3259–3270. https://doi.org/10.1029/95WR02570.

Shannon CE. 1948. A mathematical theory of communication. *Bell system technical journal*, 27(3): 379–423.

Silliman SE. 1996. The importance of the third dimension on transport through saturated porous media: case study based on transport of particles. *Journal of Hydrology*, 179(1): 181–195. https://doi.org/10.1016/0022-1694(95)02838-2.

Soares A. 1998. Sequential Indicator Simulation with Correction for Local Probabilities. *Mathematical Geology*, 30(6): 761–765. https://doi.org/10.1023/A:1022451504120.

Strebelle S. 2002. Conditional Simulation of Complex Geological Structures Using Multiple-Point Statistics. *Mathematical Geology*, 34(1): 1–21. https://doi.org/10.1023/A:1014009426274.

Tartakovsky DM. 2013. Assessment and management of risk in subsurface hydrology: A review and perspective. *Advances in Water Resources*, 51: 247–260. https://doi.org/10.1016/j.advwatres.2012.04.007.

Truex MJ, Johnson CD, Becker DJ, Lee MH, Nimmons MJ. 2015. *Performance Assessment for Pump-and-Treat Closure or Transition. Document PNNL-24696.* Pacific Northwest National Lab (PNNL), Richland, WA (United States).

Wang M, Zheng C. 1997. Optimal Remediation Policy Selection under General Conditions. *Groundwater*, 35(5): 757–764. https://doi.org/10.1111/j.1745-6584.1997.tb00144.x.

Wiegand R, Shanahan F. 2001. Cost analyses for selected groundwater cleanup projects: pump and treat systems and permeable reactive barriers. .

Yang Y-L, Reddy KR, Zhang W-J, Fan R-D, Du Y-J. 2020. SHMP-Amended Ca-Bentonite/Sand Backfill Barrier for Containment of Lead Contamination in Groundwater. *International Journal of Environmental Research and Public Health*, 17(1): 370. https://doi.org/10.3390/ijerph17010370.

Zinn B, Harvey CF. 2003. When good statistical models of aquifer heterogeneity go bad: A comparison of flow, dispersion, and mass transfer in connected and multivariate Gaussian

hydraulic conductivity fields: FLOW, DISPERSION, AND MASS TRANSFER. *Water Resources Research*, 39(3). https://doi.org/10.1029/2001WR001146.